Journal Pre-proofs

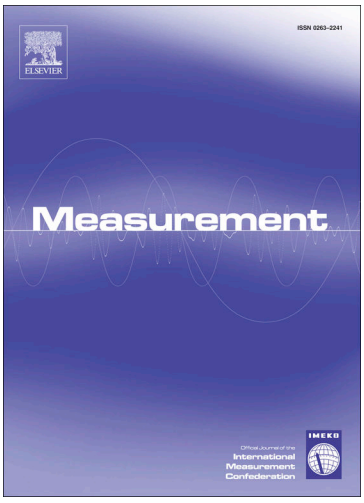

Localizing Damage on Stainless Steel Structures Using Acoustic Emission Signals and Weighted Ensemble Regression-based Convolutional Neural Network

Li Ai, Mahmoud Bayat, Paul Ziehl

PII: S0263-2241(23)00223-3
DOI: https://doi.org/10.1016/j.measurement.2023.112659
Reference: MEASUR 112659

To appear in: *Measurement*

Received Date: 7 November 2022
Revised Date: 21 February 2023
Accepted Date: 24 February 2023

Please cite this article as: L. Ai, M. Bayat, P. Ziehl, Localizing Damage on Stainless Steel Structures Using Acoustic Emission Signals and Weighted Ensemble Regression-based Convolutional Neural Network, *Measurement* (2023), doi: https://doi.org/10.1016/j.measurement.2023.112659

Localizing Damage on Stainless Steel Structures Using Acoustic Emission Signals and Weighted Ensemble Regression-based Convolutional Neural Network

Li Ai[1], Mahmoud Bayat[1*], Paul Ziehl[1,2]

[1] Department of Civil and Environmental Engineering, University of South Carolina, Columbia, SC, USA

[2] Department of Mechanical Engineering, University of South Carolina, Columbia, SC, USA

[1*]Corresponding author, Ph.D., Research Associate Professor, E-mail: mbayat@mailbox.sc.edu

Localizing Damage on Stainless Steel Structures Using Acoustic Emission Signals and Weighted Ensemble Regression-based Convolutional Neural Network

Abstract

Nuclear power generation is an essential part of the electrical supply in the United States, and it is an effective way to achieve low carbon power generation. Nuclear power generation produces spent radioactive fuel. If improperly disposed of or improperly stored, spent fuel can affect the environment and human health. Currently, in the United States, spent fuel is typically stored in stainless steel canisters. Some stainless steel canisters deployed in coastal areas are subject to stress corrosion cracks. Long-term monitoring and to provide timely maintenance of the storage canisters is necessary to prevent leakage of spent fuel due to damaged canisters. Acoustic emission (AE) is a structural health monitoring (SHM) technique that can be utilized to monitor large-scale metallic structures because it is extremely sensitive to damage initiation and propagation in materials. However, the challenge in using AE is in deploying a minimal number of AE sensors on a canister due to cost and environmental restrictions while still being able to precisely detect and localize damage formation. The innovation of this paper lies in the development of an automated damage localization method to estimate the coordinates of damage by using a single AE sensor. A data fusion approach was designed to integrate the information from waveforms, fast Fourier transform (FFT) spectrums, and spectrum entropy and then convert the AE signals into three types of images along with short-time Fourier transform (STFT) and continuous wavelet transforms (CWT). A weighted ensemble regression-based convolutional neural network was proposed to analyze the images and compute the coordinates of damage. The proposed method was validated on a large-scale steel plate specimen that simulate the canister, and three-fold cross-validation was conducted to ensure the method was effectively evaluated. The results suggest that the proposed method has a high performance rate for locating damage.

Keywords: Acoustic emission; Spent fuel storage canister; Source localization; Convolutional neural network

1. Introduction

Stainless steel is one of the most commonly utilized materials in infrastructure systems such as nuclear power facilities. Currently, spent fuel is stored in stainless steel canisters in the United States [1-3]. Welding is used to seal the top of the canister. Afterward, the entire canister is covered by a concrete overpack to avoid radioactive leakage [4]. The canisters, however, are potentially vulnerable to structural damage from stress corrosion cracking (SCC) due to the combined influence of residual stresses in the welded area at the top of the canisters and the high humidity and salinity of the

environment in the coastal area where the canisters are stored [5]. This poses a significant threat to public safety. Therefore, inspecting the canisters, locating the damaged area(s), and providing informed maintenance on a regular basis are beneficial. Due to the sensitive nature of the spent fuel storage system, destructive detection is not desirable. Traditional nondestructive methods, including regular visual inspections, are often time-consuming and prone to human error. Furthermore, a visual inspection can be challenging to accomplish as the surface of the canister is covered with a concrete overpack. An automated nondestructive monitoring approach is desired to improve the feasibility and effectiveness of damage detection on the canister.

Several nondestructive approaches, such as radiographic inspection [6], ultrasonic testing [7], acoustic emission (AE) [8-10], and thermal imaging/infrared [11; 12], have been employed in the inspection and monitoring of infrastructural components. AE is an approach worth studying among those approaches as it is sensitive to damage formation and propagation on the surface or inside the material [13-15]. The AE signal is generated by the rapid release of damage-induced elastic energy when the damage occurs [16]. By attaching the AE sensor to the surface of the object, the AE signal is detected and recorded by the data acquisition system. The source localization of the damage can be conducted by deploying an array of sensors. Research related to AE sensor arrays has been widely conducted [17-19]. Holford et al. [17] utilized the AE sensor array and time of arrival (TOA) approach to detect and localize the defects on metallic landing gear components. The proposed approach was proved to be effective on a full-scale steel landing gear component undergoing fatigue loading. Soltangharaei et al. [18] studied the localization and identification of SCC damage on a 304 stainless steel plate by using the TOA approach and an unsupervised pattern recognition algorithm. AE signals induced by SCC were recorded by an AE sensor array including eight sensors. Khyzhniak et al. [19] proposed to use the AE sensor array and time difference of arrival (TDOA) method, an improved method based on TOA, to localize the sources in 2-dimensional space. The firefly algorithm and the gradient descent algorithm were adopted to assist in calculating the coordinates of the AE sources. The results show that the position of the AE sources can be accurately located.

Previous studies indicated that AE monitoring with multiple sensors has a good capability for detecting and identifying damages in specimens. However, the practical implementation of AE sensor arrays in realistic spent fuel storage canisters presents obstacles. The available area of the canisters where AE sensors can be deployed is limited as the canisters are covered by concrete overpacks. Therefore, sensors are usually positioned on the base support structure [4]. Damage produced by SCC, on the other hand, mainly occurs in the welded area near the top of the canister. Therefore, it is not feasible to locate damage on the spent fuel canister by deploying the AE sensor array around the damaged area. Adopting as few AE sensors as possible and conducting the source localization with artificial intelligence techniques may be a promising approach.

Machine learning is a branch of artificial intelligence techniques. Machine learning relies on studying the features extracted from large amounts of data, finding patterns in the data, and then leveraging those patterns to make predictions without

human interpretation [20-23]. Deep learning is a technique that builds on the basis of machine learning. Instead of conducting feature engineering on the input data, it automatically extracts features from the raw data [24-27]. Machine learning and deep learning have been utilized in many studies in signal processing, such as anomaly detection in human electrocardiogram (ECG) signals [28; 29], the diagnosis of machine failure conditions [30; 31], and the analysis of seismic signals [32]. Recently, machine learning and deep learning have also been applied to AE source localization. Ebrahimkhanlou et al. [33] proposed an AE source localization method to predict AE source coordinates by deploying a sensor array and a stacked autoencoder network. Ai et al. [34] developed a passive health monitoring system to conduct zonal impacts localization on an aircraft component using one AE sensor. Random forest and stacked autoencoder networks were utilized to analyze the signals from one sensor.

Previous studies have proven that using machine learning and deep learning to localize AE signals can be promising and could be an option to localize SCC damage on spent fuel storage canisters. However, most current studies of AE source localization using machine learning and deep learning utilized sensor arrays to predict the source coordinates [33], and employed a single AE sensor for zonal localization [34; 35]. An AE single-sensor localizing methods using stacked denoising autoencoders was developed in [36] to estimate the coordinates. This study was carried out on a small-scale plate (800 mm × 800 mm × 3.2 mm). The signals were not heavily attenuated and the AE sensor with the high operating frequency range (such as PK15I, with operating frequency from 100-450 kHz) can be used, so that the received AE signal can contain valid information in the 100-400 kHz frequency band. However, in the field application, the spent fuel storage canisters are relatively large in size (over 5000 mm in height), the elastic wave can be severely attenuated when transmitted over such long distances. Some useful information relating to the location of the source may be lost in the wave propagation process. On the other hand, the sensitive low-frequency resonance sensors (with operating frequency less than 100 kHz) are generally used to ensure that the AE signal can be received over long distances. This results in the received signal containing very few information in the 100-400 kHz band. The two points mentioned above result in a large amount of important information being missing from the signals received by single-sensors on large structures. Therefore, a more efficient algorithm is needed to extract deeper effective features from the residual information of the signals and estimate the AE source coordinates on the large-scale specimen. Currently, no research has been done to accomplish this. To fill the gap, this paper proposes a weighted ensemble regression-based convolutional neural network (WER-CNN) for source localization on large-scale spent fuel storage canisters using minimal number of AE sensor. The main contributions of this paper are: (1) A dataset of AE signals created by conducting pencil-lead-break (PLB) experiments on the specimen to simulate SCC damage; (2) a new signal fusion method named WFE-fusion is proposed to fuse the original waveform, FFT spectrum, and spectral entropy of each AE signal and convert them into RGB images; (3) each AE signal was converted to three RGB images via three methods: WFE-fusion, Short-time Fourier transform, and continuous wavelet transforms. A WER-CNN was developed to comprehensively learn the information of

three RGB images and calculate the coordinates of the signal source; (4) The proposed WER-CNN is compared with other methods based on root mean square error (RMSE), R^2, and standard deviation.

The rest of the paper is organized as follows. Section 2 presents the experimental setup, including the introduction of the specimen and the AE setup. Section 3 presents the proposed source localization method and its implementation procedure. Section 4 discussed the performance of the proposed method. The conclusions are summarized in Section 5.

2. Experimental Setup and Procedures

A large-scale 304H stainless steel plate specimen, as shown in Fig. 1, was manufactured for this study. To simulate the actual spent fuel storage canister, the large-scale specimen has a very similar thickness and length to the actual canister. The dimensions of the large-scale steel plate are 5029 x 1524 x 16 mm. In addition to the large-scale steel plate, two bolted small steel plates were fabricated and attached to the large-scale specimen to simulate the circumstance where the canister is placed on the bottom support. A certain torque is applied to the bolt to mimic the pressure from the weight of an actual canister. To match the practical situation where an AE sensor could only be attached to the bottom support, one AE sensor was placed on one of the bolted small steel plates during the entire experiment. This experiment is a preliminary verification of the method proposed in this paper in a laboratory environment. Experiments performed on actual canisters will be covered in future studies.

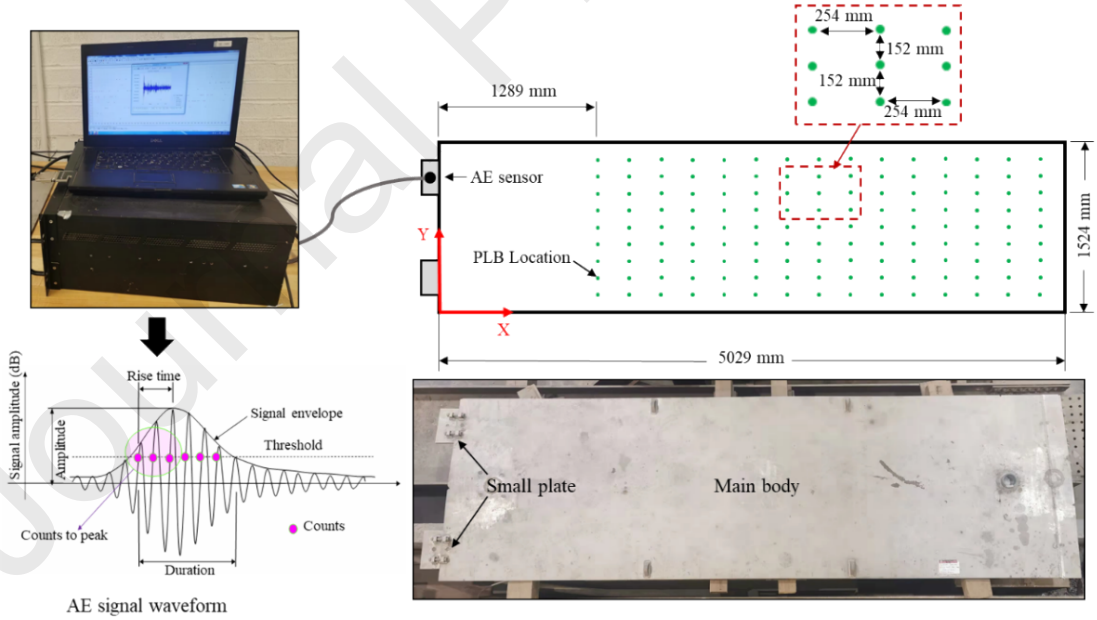

Fig. 1. Specimen and experimental setup

The Hsu-Nielsen pencil-lead-break (PLB) is commonly used to generate AE signals [37]. PLB signals and the actual SCC signals have some similarities, but the difference still exists. The focus of this paper is to preliminarily verify the proposed localization method. PLB signals are easy to obtain and easy to reproduce. Therefore,

in this paper, Hsu-Nielsen PLB was performed on the large-scale plate to simulate the SCC damage occurring on the cylinder. The future work would focus on reducing the difference between the PLB and SCC signals using domain adaptation technique.

The pre-marked positions to conduct PLB (green dots) were evenly distributed in the area near the right side of the plate. All the green dots and their spacing are presented in Fig. 1. The lower-left corner of the large-scale plate is employed as the origin of the Cartesian coordinate system. Each green dot is given a coordinate (x, y) with this point as the origin. The PLB was repeated 30 times on each green dot throughout the experiment. All of the AE signals induced by the PLB were captured by the single AE sensor on the small plate and recorded by the AE acquisition system. A scheme of a typical AE waveform is presented in Fig. 1.

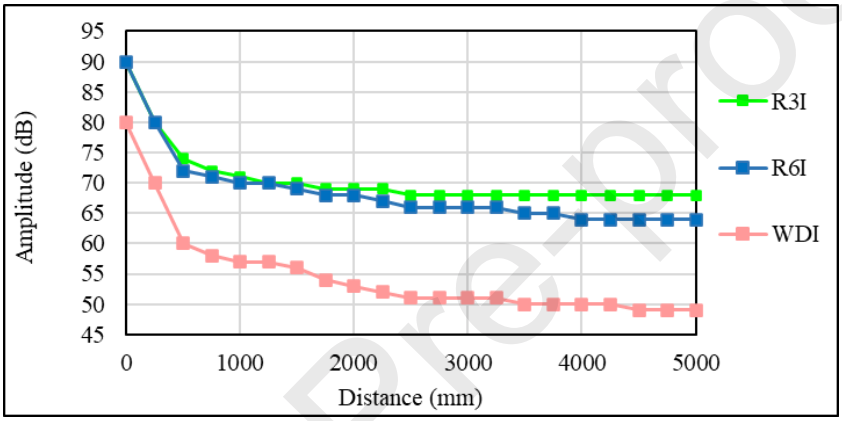

Fig. 2. Attenuation curves of three types of AE sensors

The AE sensor and the acquisition system were produced by the MISTRAS Group Inc., Princeton Junction, New Jersey. To determine the appropriate AE sensor used in this experiment, an attenuation test has been conducted on three types of AE sensors. These sensors are the WDI sensor with an operating frequency range of 100-900 kHz, the R6I sensor with an operating frequency range of 40-100 kHz, and the R3I sensor with an operating frequency range of 10-40 kHz. The steel plate specimen was subjected to PLB at distances between 0 and 5000 mm from the sensor. Fig. 2 shows the outcomes. The AE sensor and the acquisition system were produced by the MISTRAS Group Inc., Princeton Junction, New Jersey. To determine the appropriate AE sensor used in this experiment, an attenuation test has been conducted on three types of AE sensors. These sensors are the WDI sensor with an operating frequency range of 100-900 kHz, the R6I sensor with an operating frequency range of 40-100 kHz, and the R3I sensor with an operating frequency range of 10-40 kHz. The steel plate specimen was subjected to PLB at distances between 0 and 5000 mm from the sensor. Fig. 2 shows the outcomes. The R3I sensor was used in this paper due to its relatively higher sensitivity over long distances, even though its operating frequency band is not directly related to the primary frequency band of the damage signal in stainless steel stress corrosion cracking, which typically falls within the 100-300 kHz range [18]. This is because the characteristics of AE signals generated from various locations on the structure are not only exhibited in

the primary frequency band. Instead, they also exhibit different reverberation patterns due to the reflection of edge waves. The reverberative, and dispersive characteristics of AE waveforms are manifested in the low frequency components of the AE signals, which can be captured by the R3I sensor. The algorithm presented in this paper is designed to extract valuable information regarding the reverberation pattern of the acoustic emission signal that has only low frequency band components and has experienced significant propagation losses.The PLB signal generated near one edge of the specimen can be well received even if the sensor is mounted on the small plate attached to the other edge of the specimen. The AE signals were recorded by a 16-channel DISP system. The details regarding the AE acquisition parameters are presented in Table 1.

Table 1. AE acquisition parameters

Acquisition parameters	**Value**
Hit Definition Time	400 μs
Peak Definition Time	200 μs
Hit Lockout Time	400 μs
Sampling Rate	1 MHz
Threshold	32dB
Pre-trigger Time	256 μs
High Pass Digital Filter	20 kHz
Low Pass Digital Filter	400 kHz

3. Methodology

3.1. Implementation procedure

The damage detection and localization method for spent fuel canisters is developed based on single-sensor AE monitoring and a weighted ensemble regression-based convolutional neural network (WER-CNN). The original AE signals extracted from the acquisition system were one-dimensional time series. This paper employed two commonly used methods: short-time Fourier transform (STFT) and continuous wavelet transforms (CWT), to convert the one-dimensional time series into RGB images while preserving the essential information. In addition to the two methods above, a data fusion method named WFE-fusion was proposed to fuse the information from the AE waveform, fast Fourier transform (FFT) spectrum, and spectral entropy. The fused information was also converted to the RGB images. In total, three different RGB images can be obtained from one AE signal. Those images are stored in an image dataset and used as the input to the WER-CNN (Details of WER-CNN is introduced in Section 3.3.4). The final output is the damage source coordinates (x, y). Fig. 3 shows the framework of the proposed source localization method.

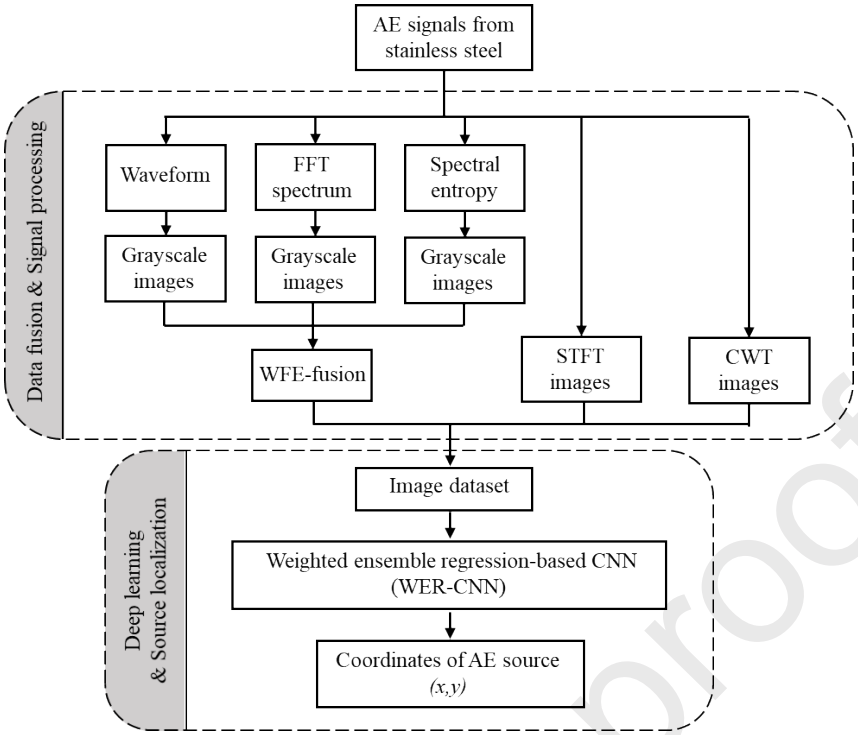

Fig. 3. Implementation procedures

3.2. AE signals pre-processing and data fusion

3.2.1. WFE-fusion

This paper proposes WFE-fusion to integrate information from the AE waveform, FFT spectrum, and spectral entropy of each AE signal. The name is the first letters of the waveform (W), FFT spectrum (F), and Entropy (E). As mentioned before, the original AE signals are one-dimensional time series. The time-domain waveform (normalized from 0 to 1) of a typical AE signal is shown in Fig 4a.

Fast Fourier transform (FFT) is a common method for transferring a signal from a time-domain waveform to a frequency-domain spectrum [38]. The discrete version of Fourier transform is utilized for digital waveforms, which is referred to as Discrete Fourier Transform (DFT), and is presented in the following Eq. (1):

$$X(m) = \sum_{n=0}^{N-1} X_n e^{-\frac{j2\pi mn}{N}} \quad (1)$$

Where, N is the number of samples. X_n is a signal in a time domain, and $X(m)$ is Fourier transform coefficients for m^{th} frequency. FFT is a fast and efficient way of computing the DFT using computers. The FFT spectrum (magnitude normalized) of the typical AE signal is presented in Fig. 4b.

Entropy is a thermodynamic concept that represents the property of a system to evolve to an internal steady state when it is not subject to external disturbances [39]. Information entropy draws on the concept of entropy in thermodynamics, which measures the uncertainty of information in signals [40-42]. A high information entropy represents a high uncertainty for a signal, and the level of information contained in the signal is low. In other words, the more disorderly the signal is (close to white noise),

the higher the information entropy is for that signal. When the information entropy of a segment in a signal suddenly decreases, it means that the segment contains special information. AE signals were converted into power spectral entropy in this study. The probability distribution of the power spectrum in a signal can be obtained by Eq. (2):

$$P(m) = \frac{X(m)^2}{\sum_i X(i)^2} \tag{2}$$

Where, $X(m)$ is Fourier transform coefficients for mthfrequency from Eq. (1). $P(m)$ refers to the probability distribution of the power spectrum for mth frequency. The spectral entropy can be calculated by substituting Eq. (2) into Eq. (3):

$$E = -\sum_{m=1}^{N} P(m)\log_2 P(m) \tag{3}$$

The instantaneous spectral entropy can be computed by the following equations:

$$E(t) = -\sum_{m=1}^{N} P(t,m)\log_2 P(t,m) \tag{4}$$

$$P(t,m) = \frac{X(t,m)^2}{\sum_f X(t,f)^2} \tag{5}$$

Where, $E(t)$ is the spectral entropy at time t. $P(t,m)$ is the probability distribution at time t. $X(t,m)$ refers to the probability distribution of the power spectrum at time t. $X(t,f)$ is the time-frequency power spectrogram. The instantaneous spectral entropy (magnitude normalized) of the typical AE signals is presented in Fig. 4c.

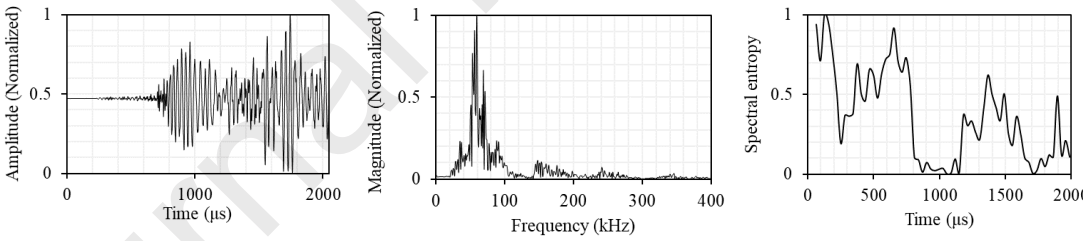

(a) (b) (c)

Fig. 4. Typical AE signal: (a) waveform; (b) FFT spectrum; (c) Spectral entropy

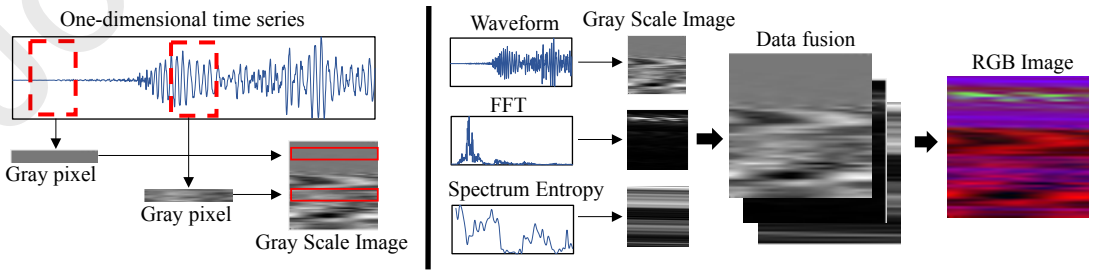

Fig. 5. Procedures of WFE-fusion

It can be observed that AE waveforms, FFT spectrum, and spectral entropy are all individual one-dimensional series. To integrate the information embedded in these

three individual series and also to meet the input requirement of the proposed WER-CNN, the series are fused to an RGB image. Figure. 5 describes the data fusion process. For each one-dimensional series, a sliding window (length L) is applied to the series to extract data and convert the numbers into gray pixel bars. The length L can be determined by the square root of the length of the series. The gray pixel bars generated by the first window is utilized as the first row of the grayscale image. Then the window continues to move backward to produce next few gray pixel bars and eventually forms a grayscale image with the size of $L \times L$. As shown in Fig 4, waveform, FFT spectrum, and spectral entropy are converted to grayscale images, respectively. To facilitate the next step of fusion, all grayscale images are reshaped to the same scale of 227×227. By stacking the reshaped grayscale images of waveform, FFT spectrum, and spectral entropy, a new RGB image with the size of $227 \times 227 \times 3$ can be built. The acquired image with the size of $227 \times 227 \times 3$ is named WFE-fusion image. Fig. 5 illustrates the WFE-fusion image of a typical AE signal.

3.2.2 Short-time Fourier transform

Short-time Fourier transform (STFT) is a commonly used method of joint time-frequency analysis [43]. Through time-frequency analysis, the time and frequency domains can be linked together. In brief, STFT uses a time window to derive the frequency spectrum at the moment of the time segment. By stacking the frequency spectrum of all segments in time order, an STFT spectrogram can be formed. The calculating process of STFT can be expressed by Eq. (6):

$$STFT(t,f) = \int_{-\infty}^{\infty} S(x)W(x-t)e^{-i2\pi f\tau}dx \tag{6}$$

Where, $W(t)$ is the window function, $S(x)$ is the signal to be transformed. The length of the window used in this paper is 300. This is determined by a trial-and-error test. In this paper, AE signals recorded from the specimen were converted to STFT spectrograms and saved as RGB STFT images with the size of $227 \times 227 \times 3$.

3.2.3 Continuous wavelet transforms

Another commonly utilized joint time-frequency analysis method is wavelet transformations [44]. One of the wavelet transformations approaches: CWT, is utilized in this study. It is able to capture and emphasize the time-frequency features in non-stationary signals [45]. The CWT process of a signal $s(t)$ can be presented as Eq. (7):

$$CWT_{(a,b)} = \frac{1}{\sqrt{|a|}}\int_{-\infty}^{\infty} s(t)\psi^*\left(\frac{t-b}{a}\right)dt \tag{7}$$

Where, CWT stands for the continuous wavelet coefficients obtained from the signals, a is the scale index parameter that controls the scaling of wavelet function and has an inverse relation to frequency, b refers to the translation parameter which controls the time-shifting of wavelets. The wavelet coefficients are generated by moving wavelets with different a scale indices across entire signals. ψ^* refers to the complex conjugate of mother wavelet function ψ. Morse wavelet [46] is used as the mother wavelet

function to conduct CWT in this study. The Fourier transform of Morse wavelet can be expressed by Eq (8):

$$\Psi_{p,\,\gamma}(x) = U(x)\alpha_{p,\,\gamma}x^{\frac{p^2}{\gamma}}e^{-x^{\gamma}} \tag{8}$$

where $U(x)$ refers to the unit step, $\alpha_{p,\,\gamma}$ refers to the normalizing constant, p^2 refers to the time-bandwidth product. γ is the parameter that characterizes the symmetry of the Morse wavelet [47]. In this paper, p^2 was set as 60 and γ was set as 3.

A scalogram image can be used to express the continuous wavelet coefficients. The images of AE waveforms are utilized as an input for the CNN models inside the proposed heterogeneous ensemble learning network. A CWT scalogram image can be used to express the continuous wavelet coefficients. All the AE signals recorded in this paper were converted to CWT scalogram images and saved as RGB images with the size of 227×227×3. The CWT RGB images generated by the Morse function have been compared with the RGB images generated by the other two wavelet functions (analytical Morlet, and Bump functions). The CNN models using the images generated by Morse can yield a slightly lower RMSE. Thus, the Morse wavelet function was selected as the mother function in this paper.

The AE signal waveforms, the corresponding WFE-fusion images, STFT images, and CWT images recorded from three locations on the specimen are shown in Fig. 6. It can be observed that waveforms of the AE signals captured from different locations show different characteristics. These differences are reflected in the WFE-fusion, STFT, and CWT images.

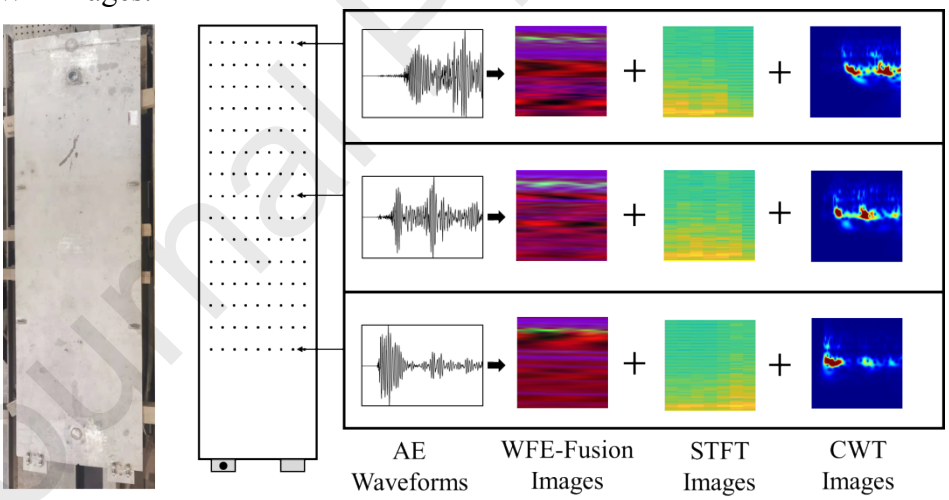

Fig. 6. WFE-fusion images, STFT images, and CWT images

3.3 Weighted ensemble regression-based convolutional neural network

CNN is a type of deep neural network that can be used to process images [48]. Through a feature extractor consisting of convolutional and pooling layers, CNN models can extract features from images and discover deep patterns in the dataset. This paper proposed a weighted ensemble regression-based convolutional neural network to analyze the AE signals and compute the coordinates of the AE sources.

As introduced in Section 3.2, the AE signals captured by the single AE sensor were converted into three image types. In order to make full use of the information from WFE-fusion images, STFT images, and CWT images, a weighted ensemble regression-based convolutional neural network (WER-CNN) was proposed to estimate the coordinates (x, y) of the damage source. The structure of the proposed ensemble network is presented in Fig. 6. WER-CNN is composed of three branches. The input for the first branch is the WFE-fusion image, the input for the second branch is the STFT image, and the input for the third branch is the CWT image. The input images are divided into training, validation, and testing datasets with a ratio of 3:1:2. In each branch, five regression-based CNN are deployed. Previous studies indicated that CNN structures like AlexNet do well in analyzing AE signals in applications such as the damage identification on railroads [49] and the crack length estimation on metallic plates [50]. To obtain a good performance in the localization of AE source, a CNN structure with a similar architecture to AlexNet is employed in each branch as the regression-based CNN. As shown in Fig. 7, the regression-based CNN has five convolution layers (Conv1 to Conv5), three max pooling layers (pool1, pool2, and pool5), three FC layers (FC6, FC7, and FC8). The dimension of the last FC layer (FC8) is modified to 1×1. A regression layer is implemented after the FC8 layer. The structure of the regression-based CNN is shown in Fig. 7. The loss function utilized in the regression layer can be expressed as Eq. (12):

$$Loss = \frac{1}{2}\sum_{i=1}^{H}(y_i' - y_i)^2 \tag{12}$$

where H refers to the number of data, y_i' stands for the target output, and y_i refers to the prediction of the regression layer.

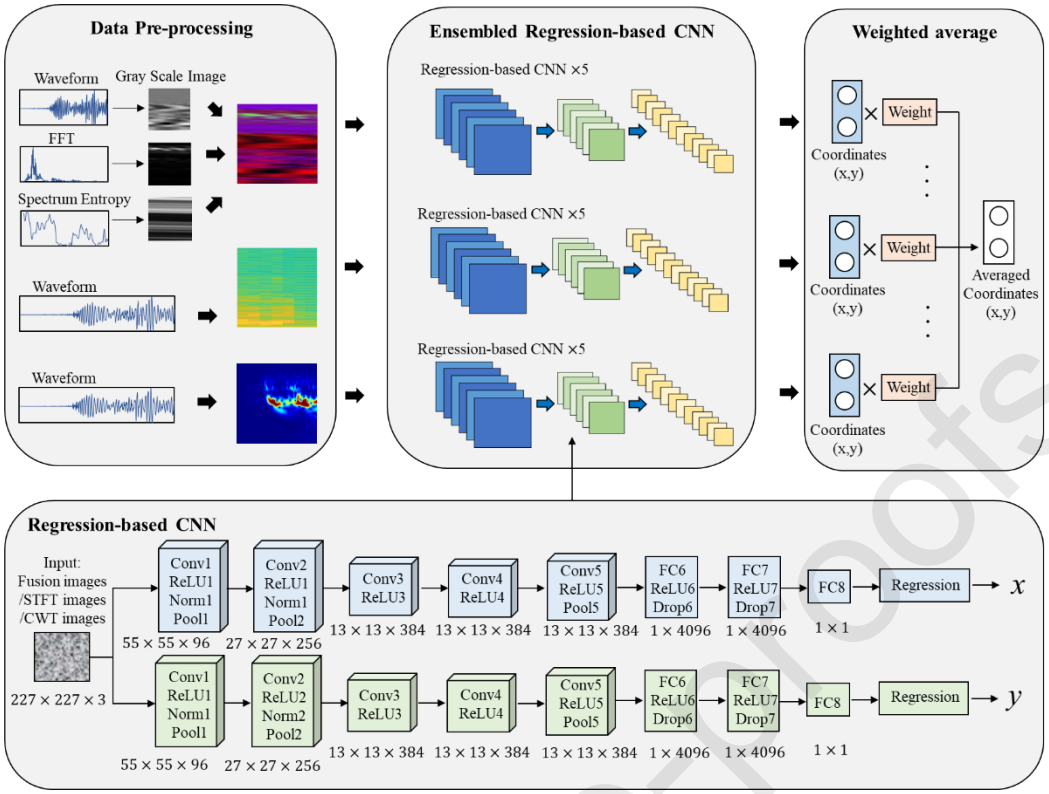

Fig. 7. Structure of the proposed WER-CNN

The regression-based CNN computes the coordinates x and y in parallel. In total, three branches and fifteen regression-based CNN are included in WER-CNN. The bagging aggregating strategy is utilized to assemble the three branches. The advantage of using bagging aggregation is that it could effectively reduce the variance and increase the accuracy of the prediction results [51]. In WER-CNN, each single regression-based CNN works independently and gives its own estimated coordinates. In total, fifteen coordinates can be obtained for one AE signal. This paper developed a weighted averaging mechanism to combine the acquired fifteen coordinates and derive the final coordinates. The weighted averaging mechanism is only implemented for the testing dataset. The weighted averaging procedure can be found in Fig. 7. The calculation of the final coordinates can be expressed by the following equation:

$$C_{final}(x,y) = \sum_{i=1}^{5} C_i(x,y) \cdot w_1 + \sum_{j=1}^{5} C_j(x,y) \cdot w_2 + \sum_{k=1}^{5} C_k(x,y) \cdot w_3 \quad (13)$$

Where, $C_i(x,y)$ refers to the coordinates given by branch 1, $C_j(x,y)$ refers to the coordinates obtained by branch 2, $C_k(x,y)$ stands for the coordinates derived by branch 3. The five coordinates obtained from each branch is assigned a weight factor: w_1, w_2, and w_3, respectively. $C_{final}(x,y)$ represents the final estimated coordinates of the damage source.

The weighting factors are obtained by considering the performance (RMSE) of each branch on the validation dataset. The following equations can be used to obtain the weighting factor:

$$w_{best} = \frac{R_{worst}}{R_{best} + R_{medium} + R_{worst}} \tag{14}$$

$$w_{medium} = \frac{R_{medium}}{R_{best} + R_{medium} + R_{worst}} \tag{15}$$

$$w_{worst} = \frac{R_{best}}{R_{best} + R_{medium} + R_{worst}} \tag{16}$$

R_{worst} refers to the RMSE of the branch with the worst performance on the validation dataset, which has the highest value. R_{medium} refers to the RMSE of the branch with a medium performance. It has the medium value. R_{best} refers to the RMSE of the branch with the best performance, which has the lowest value. Eq. (14) to Eq. (16) ensure that the worst-performing branch is assigned the lowest weight and the best performing branch is assigned the highest weight.

This paper also developed an ensemble regression-based convolutional neural network (ER-CNN). It is essentially a WER-CNN with the weighted averaging process replaced by an average process. ER-CNN was developed to compare with WER-CNN and to study the effect of the weighted averaging mechanism. The structure of the ER-CNN is shown in Fig. 8.

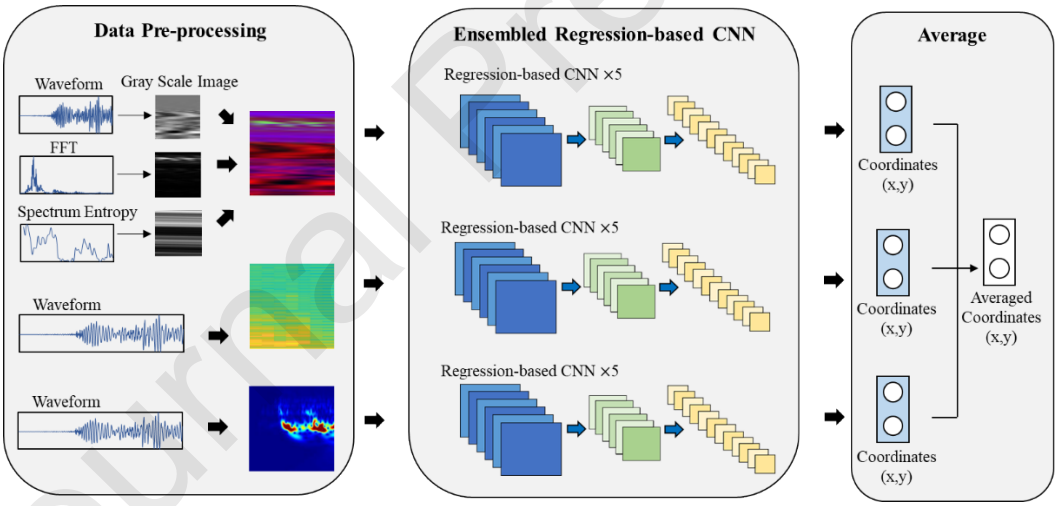

Fig. 8. Structure of ER-CNN

4. Results and Discussion

During the experiment, the PLB on each pre-marked position was repeated 30 times. In total, 4050 PLB events were detected and recorded by the AE acquisition system. The AE signals were transferred to 4050 WFE-fusion images, 4050 STFT images, and 4050 CWT images, respectively. In this section, the performance of regression-based CNNs for localization on WFE-fused images, STFT images, and CWT images are evaluated separately and compared with the performance of the proposed WER-CNN using all three types of images. Furthermore, three-fold cross-validation is conducted to verify the accuracy and effectiveness of the proposed approach. The input images are randomly divided into three subsets: A, B, and C.

This paper used three metrics, including root mean squared error (RMSE), R-squared (R2), and Standard deviation, to evaluate the source localization performance. RMSE is the square root of the mean of the square of the error between the target and the predicted value. It can be expressed as:

$$RMSE = \sqrt{\frac{1}{n}\sum_{i=1}^{n}(y_i' - y_i)^2} \tag{17}$$

where n is the number of inputs in the dataset, y_i' stands for the target value, and y_i refers to the predicted value.

R^2 refers to the proportion of the variation in the dependent variable that is predictable from the independent variables. It can measure the similarity between the targets and the predictions. R^2 can be obtained by Eq. (18):

$$R^2 = 1 - \frac{\sum_{i=1}^{n}(y_i' - y_i)^2}{\sum_{i=1}^{n}(\bar{y} - y_i)^2} \tag{18}$$

where $\bar{y}$ stands for the average of all the target values.

Stand deviation (SD) is utilized in this paper to measure the dispersion level of the estimated coordinates. It is derived by Eq. (19):

$$SD = \sqrt{\frac{1}{n}\sum_{i=1}^{n}(y_i' - \overline{y_i'})^2} \tag{19}$$

where $\overline{y_i'}$ refers to the average of all of the predicted values.

The training, validating, and testing processes for the CNN models were conducted on a workstation with a CPU-R9 5900HX, 4.6GHz, 32GB RAM, and a GPU-RTX3080, 16 GB GDDR6. For all the CNN models in this paper, the gradient descent optimization was conducted using the Adaptive moment estimation (Adam) method. The minibatch size was 35, the learning rate was 0.0001, and the maximum number of epochs was 35.

4.1 Source localization using single regression-based CNN

The training curves of the regression-based CNN using WER-fusion, STFT, and CWT images in terms of RMSE versus epochs are shown in Fig. 8. For both coordinate x and coordinate y, the RMSE of all the three curves decreases quickly in the first five epochs and then starts to converge. These three curves are highly similar; however, when zoomed in at the third epochs, it can be observed that the CNN with CWT images converges slightly faster, followed by the CNN with WFE-fusion images and then the CNN with STFT images. After convergence (e.g., at the 20th epochs), the RMSE of the CNN with CWT images is slightly lower than that of the CNN with WFE-fusion images, and the CNN with STFT images has the highest RMSE. The minor difference between the three different input images indicates they have similar source localization performance.

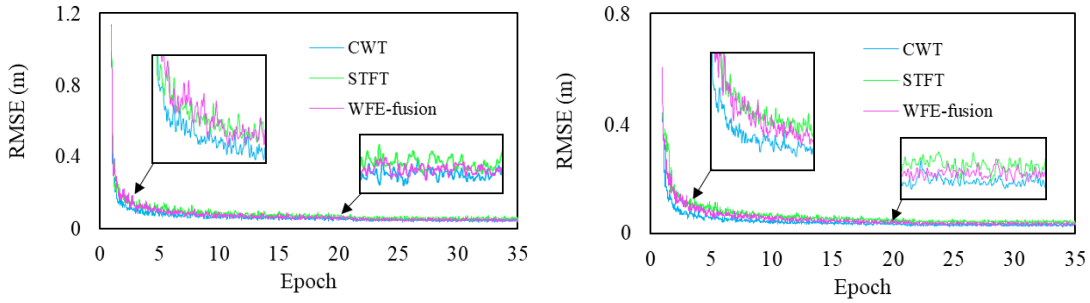

Fig. 8. Training loss of single regression-based CNN: (a) coordinate *x*; (b) coordinate *y*

After the training and validation were finished, The CNN models using three different types of images were separately tested on the 1350 testing image sets. The RMSE of coordinate *x* is 0.084 meters for STFT images, 0.079 meters for WFE-fusion images, and 0.075 meters for CWT images. For coordinate *y,* the RMSE is 0.058 meters for STFT images, 0.053 meters for WFE-fusion images, and 0.043 meters for CWT images. The results of RMSE can be found in Table 2. On the specimen with a size of 5.029×1.524 meters, all the regression-based CNN models using three types of images estimated the coordinates with an RMSE below 0.09 meters, indicating they all have acceptable performance in AE localization. And the minor difference between the three different input images indicates that their source localization performance is not significantly different.

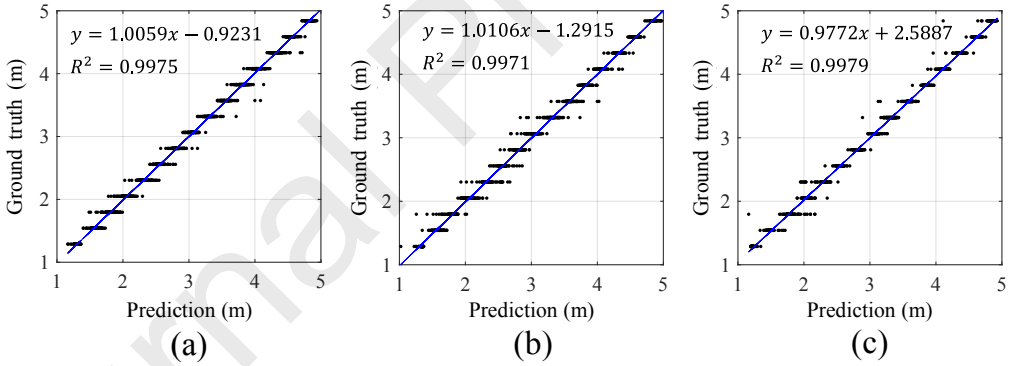

Fig. 9. Actual coordinate *x* versus estimated coordinate *x* of single regression-based CNN: (a) WFE-fusion images; (b) STFT images; (c) CWT images

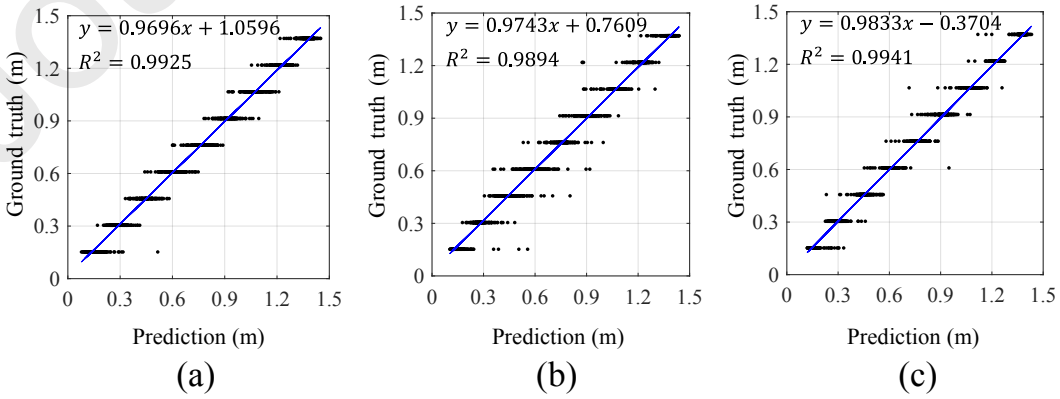

Fig. 10. Actual coordinate *y* versus estimated coordinate *y* of single regression-based CNN: (a) WFE-fusion images; (b) STFT images; (c) CWT images

Fig. 9 shows the actual coordinate x (ground truth) in the testing set and the estimated coordinate x (prediction). Fig. 10 shows the actual coordinate y and the estimated coordinate y. The R^2 between the actual and estimated x is 0.9975 for WFE-fusion images, 0.9971 for STFT images, and 0.9979 for CWT images. The R^2 between the actual and estimated y is 0.9925 for WFE-fusion images, 0.9894 for STFT images, and 0.9941 for CWT images. The results of R^2 are presented in Table 2. These results emphasize the acceptable performance in AE localization of the regression-based CNN models using three different types of images, as the values of R^2 between the actual and estimated coordinates are very close to 1. When using STFT images, the CNN model has the lowest R^2, while the R^2 of CNN using WFE-fusion and CWT images is relatively higher. The results are consistent with the observations of RMSE.

In the testing set, each PLB point has ten signals to be source localized. The dispersion of the estimated coordinates was investigated. The degrees errors and the interquartile ranges of the estimated coordinates on all 135 PLB points are presented in the box plots shown in Figs. 11 and 12. The interquartile range describes the middle 50% of values when ranking from low to high. Overall, the CNN model using STFT had a slightly higher interquartile range, while the CNN models using WFE-fusion and CWT had a lower interquartile range. The SD of the estimated coordinates was calculated. For coordinate x, the SD is 0.061 when using the CNN with WFE-fusion images, 0.063 when using the CNN with STFT images, and 0.048 when using the CNN with CWT images. The SD for coordinate y is 0.043 for WFE-fusion images, 0.045 for STFT images, and 0.035 for CWT images. All the results of SD are presented in Table 2.

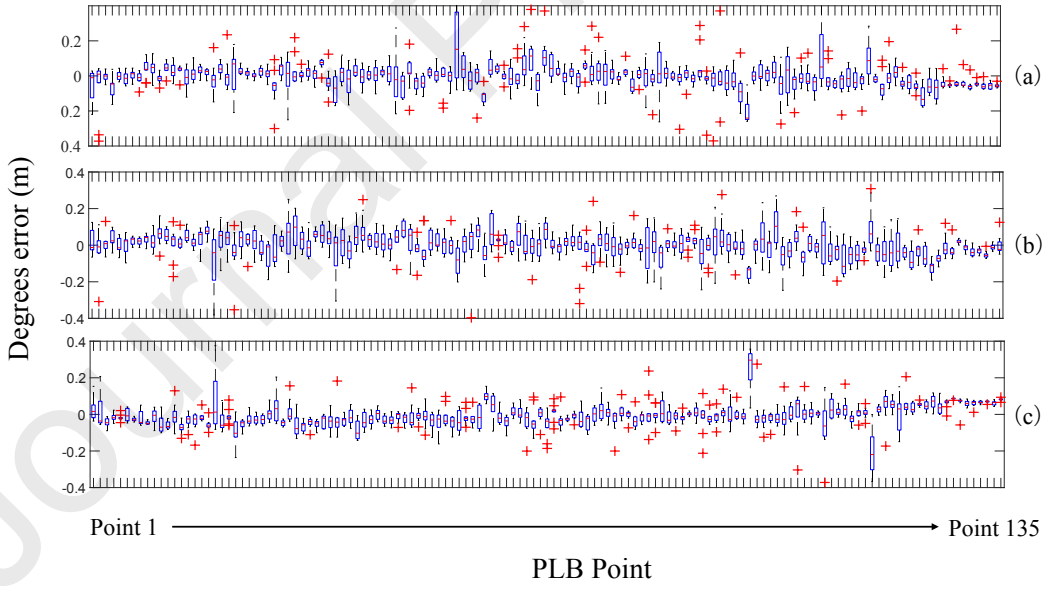

Fig. 11. Boxplot of the testing RMSE of the estimated coordinate x of single regression-based CNN: (a) WFE-fusion images; (b) STFT images; (c) CWT images

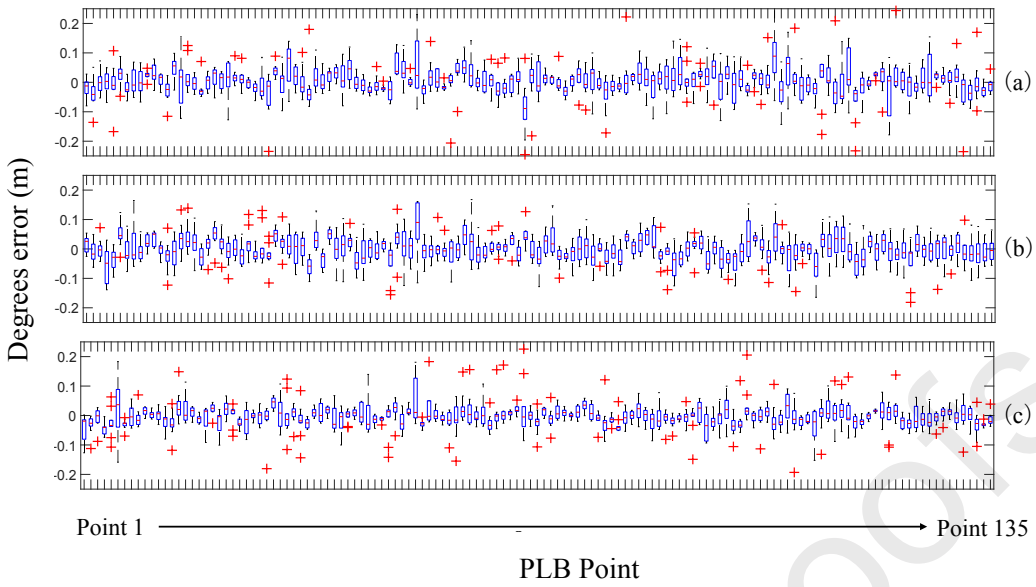

Fig. 12. Boxplot of the testing RMSE of the estimated coordinate *y* of single regression-based CNN: (a) WFE-fusion images; (b) STFT images; (c) CWT images

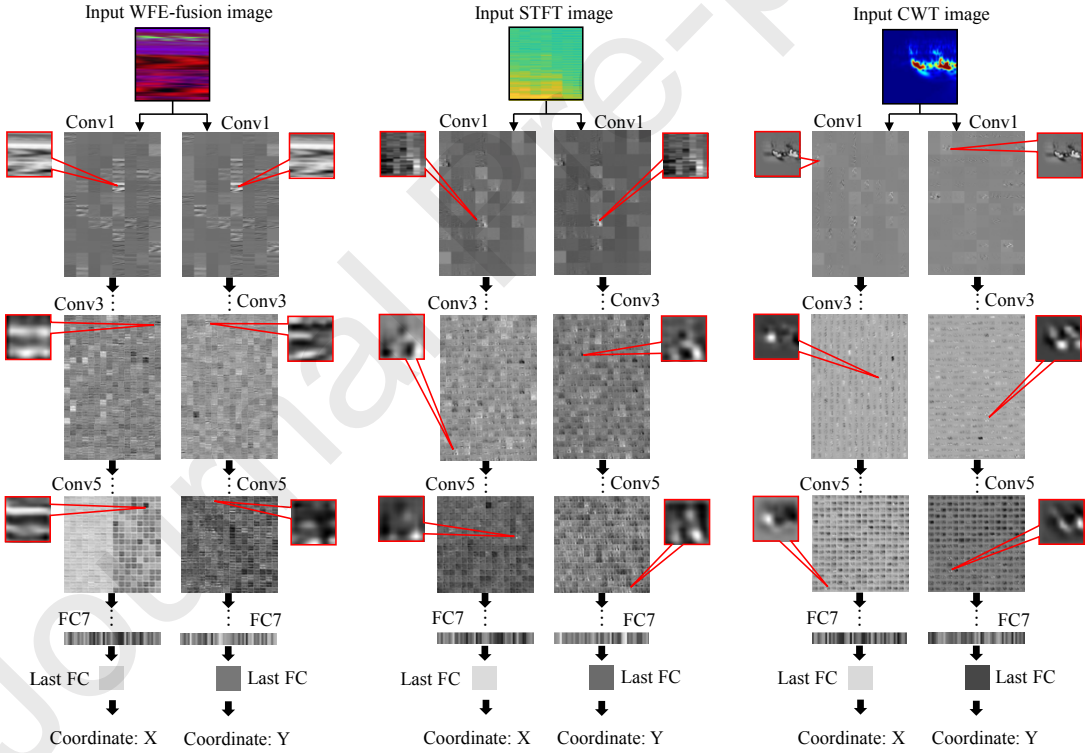

Fig. 13. Visualization of feature extraction process

The automated feature extraction processes of the regression-based CNN models using three types of input images were shown by visualizing the activation maps in convolutional and FC layers. The first, the third, and the fifth convolutional layers, the FC7 layer, and the last FC layer are selected to illustrate the activation maps. Each activation map is composed of multiple small tiles, which refer to the output of several channels during the feature learning process. The light and white pixels in the activation map represent positive activations. A lighter color represents a stronger positive

activation. On the other hand, negative activation is represented by dark and black pixels, and the darker the color, the stronger the negative activation. In Fig. 13, the tiles with the strongest channel are magnified and indicated by red boxes. It can be observed from the figure that the shallow convolutional layer learns the basic features, such as the contours of the frequency components in the image. More complex features related to the coordinates of the AE source are learned in deeper layers. And it is obvious that the feature maps learned from the three types of images for one AE signal were significantly different from each other. However, the outputs of the last FC layer (FC8) are very similar. These observations illustrate that the regression-based CNN can effectively extract information automatically and eventually learn similar information about the coordinates of the AE source from the three images generated from the same AE signal.

4. 2. Source localization using WER-CNN

The source localization performance of the proposed WER-CNN is investigated in this section. All the fifteen regression-based CNN models in branches 1, 2, and 3 are trained and validated individually and form the ensemble network. The source localization results on the testing AE signals are also evaluated by the metrics: RMSE, R^2, and SD. The RMSE of coordinate x generated by WER-CNN is 0.054 meters. The RMSE of coordinate y is 0.032 meters. Compared to any of the single regression-based CNN models (0.084 for STFT, 0.079 for WFE-fusion, and 0.075 for CWT), a sizable RMSE reduction can be observed. The actual coordinates versus the estimated coordinates can be discovered in Fig. 14. The R^2 between the actual and estimated coordinate x computed by WER-CNN is 0.9985. The R^2 between the actual and estimated coordinate y is 0.9962. There is an improvement in the R^2 when compared with the single regression CNN models in Section 4.1.

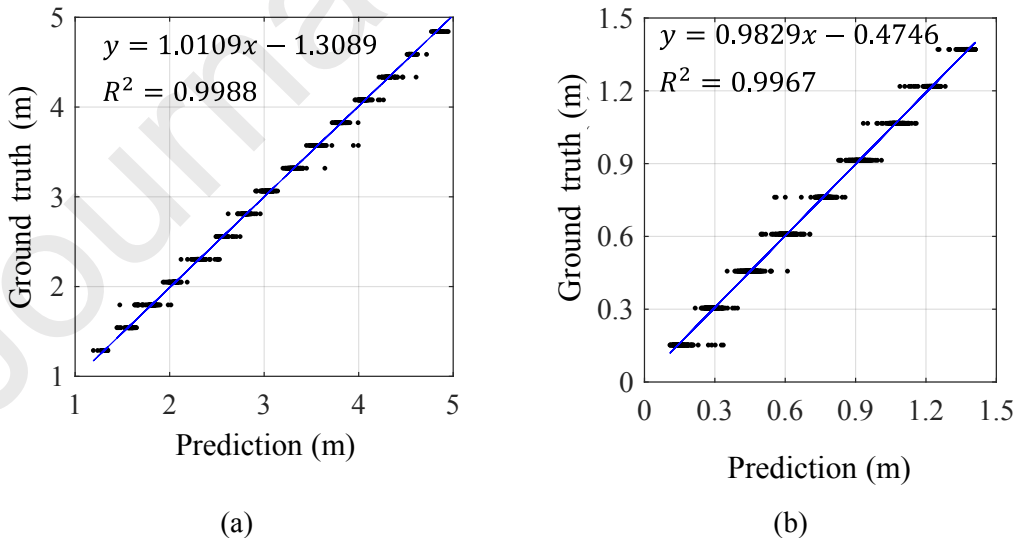

(a) (b)

Fig. 14. Actual coordinates versus estimated coordinates of WER-CNN: (a) coordinates x; (b) coordinates y

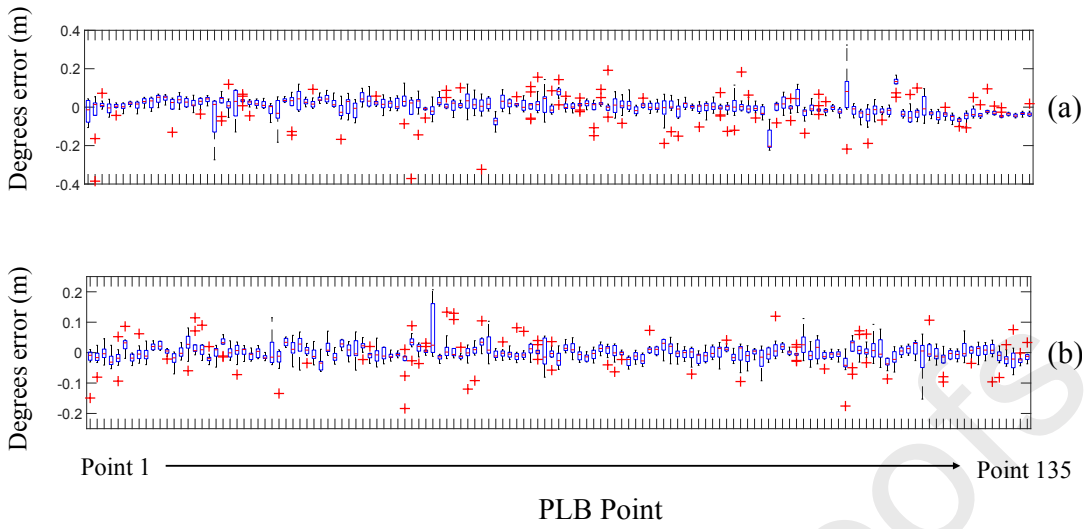

Fig. 15. Boxplot of the testing RMSE of the estimated coordinates given by WER-CNN: (a) coordinates *x*; (b) coordinates *y*

Fig. 15 presents the box plots that show the degree errors and the interquartile ranges of the coordinates estimated by WER-CNN. Notably, the WER-CNN model has a lower interquartile range than the single regression-based CNN models. The SDs of the estimated coordinates are computed to evaluate the dispersion of results. When using the WER-CNN, the SD is 0.036 for coordinate *x*, 0.024 for coordinate *y*. A significant decrease in SD can be observed after using WER-CNN.

Table 2. Performance comparison

Metrics		RMSE	R^2	SD
CNN	*x*	0.084	0.9975	0.061
Input: STFT	*y*	0.058	0.9925	0.043
CNN	*x*	0.079	0.9971	0.063
Input: Fusion	*y*	0.053	0.9894	0.045
CNN	*x*	0.075	0.9979	0.048
Input: CWT	*y*	0.043	0.9941	0.035
Branch of five CNNs	*x*	0.078	0.9977	0.058
Input: STFT	*y*	0.053	0.9930	0.040
Branch of five CNNs	*x*	0.072	0.9974	0.059
Input: Fusion	*y*	0.049	0.9911	0.043
Branch of five CNNs	*x*	0.070	0.9981	0.046
Input: CWT	*y*	0.042	0.9943	0.034
ER-CNN no weighting	*x*	0.056	0.9985	0.037
	y	0.035	0.9962	0.026
WER-CNN with weighting	*x*	0.054	0.9988	0.036
	y	0.032	0.9967	0.024

To study the effect of the weighted averaging mechanism utilized in WER-CNN, an ensemble regression-based convolutional neural network (ER-CNN) without the weighted averaging mechanism is developed and tested. All the results of ER-CNN and WER-CNN, including RMSE, R^2, and SD are listed in Table 2. The performance of WER-CNN using the weighted averaging mechanism is better than that of ER-CNN without using mechanism. This proves the effectiveness of the weighted averaging mechanism.

The localization performances of the branches (five regression-based CNN models using one type of image) were also studied. The coordinates provided by the five CNN models in one branch were averaged to derive the eventual coordinates. The localization efficiencies were also evaluated by RMSE, R2, and SD. Results can be found in Table 2. It can be observed that averaging the localization results using one type of image can improve the localization performance over the single CNN to a certain extent. While The WER-CNN utilized in this paper can improve the localization performance more significantly by comprehensively considering three different types of images.

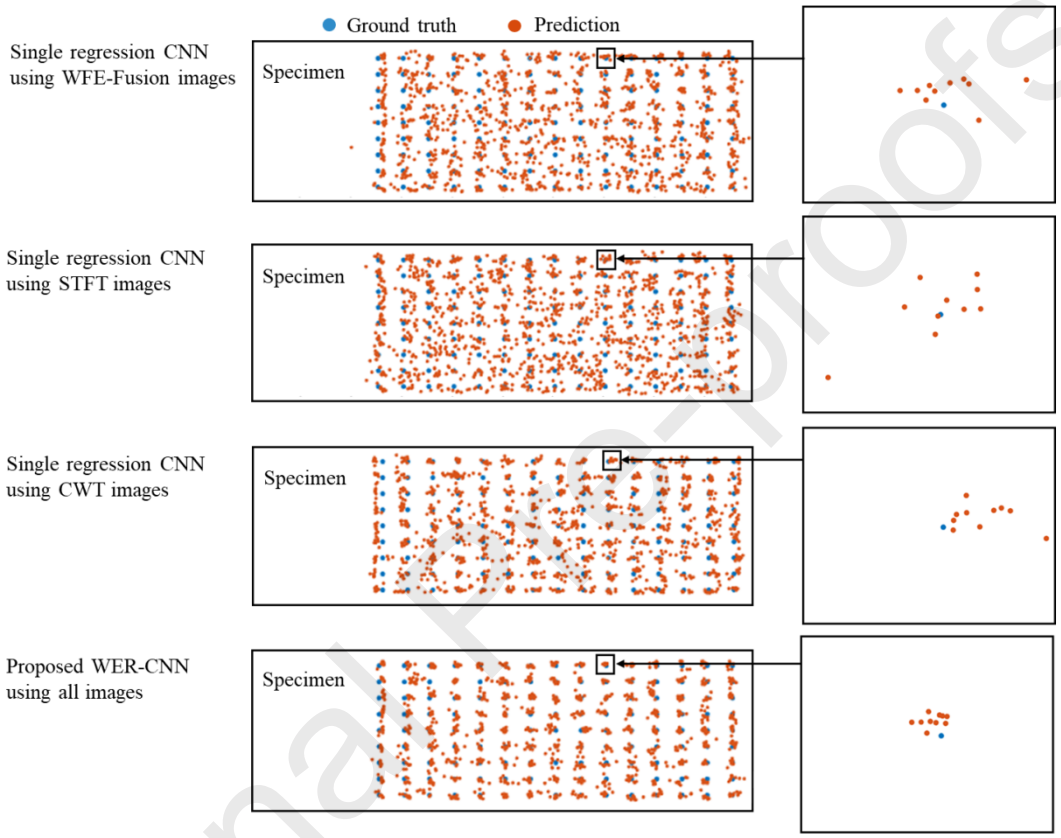

Fig. 16. Visualization of the actual and estimated coordinates on the specimen

To better visualize the performance of AE source localization, the estimated coordinates of the AE source and the actual coordinates are compared and illustrated in Fig. 16. The blue dots represent the actual locations of PLB, and the red dots stand for the estimated locations. It can be seen that the regression-based CNN models with different images and the WER-CNN proposed in this paper that comprehensively uses all images can both estimate the coordinates of AE sources. However, there are significant differences in the distance between the obtained estimated coordinates and the actual coordinates, as well as in the dispersion of the estimated coordinates. The figure shows that the single regression-based CNN using STFT images has the highest discreteness, followed by the CNN models using CWT images and WFE-fusion images, and the proposed WER-CNN has the lowest discreteness compared to the three single regression-based CNN models. This observation is consistent with the previous findings of SD (shown in Table 2). One of the 135 PLB points is zoomed in to show more detail between the actual and estimated coordinates. This is intended to give a

more intuitive view of the improvement of source localization on this point brought by the proposed method. The coordinates obtained by the single regression-based CNN models are scattered around the actual coordinates to a certain extent, while the coordinates estimated by WER-CNN are more closely clustered around the actual coordinates. In addition, it can also be seen from the figure that the coordinates given by WER-CNN are closer to the actual coordinates compared with other single regression-based CNN models. This finding is also aligned with previous RMSE observations.

The paper also compared the proposed WER-CNN with an existing location method with single AE sensor: localization using stacked denoising autoencoders (SDAE) [36]. The input of the SDAE was the AE waveforms adding gaussian white noise with 15 signal power. The SDAE used in the comparison has two denoising autoencoders. The first denoising autoencoder has a hidden size of 100, and the second one has a hidden size of 50. The training/validation/testing ratio was kept the same with WER-CNN. The RMSE of SDAE, the three single-CNN models using different input, and WER-CNN are presented in Table 3. The single-CNN models and WER-CNN have lower RMSE than SDAE. The difference in the performance of SDAE and the methods in this paper may be due to the difference in the ability of feature extraction. This founding demonstrated the advance of the proposed method in this paper.

Table 3. RMSE of the proposed and the existing method

Models	RMSE of x	RMSE of y
SDAE	0.097	0.069
CNN using STFT	0.084	0.058
CNN using WFE-fusion	0.079	0.053
CNN using CWT	0.075	0.043
WER-CNN	0.054	0.032

4. 3. Three-fold cross-validation

The model evaluation results presented above are based on a specific training/testing division. It is unknown whether the results of the model are related to the way in which the training and testing sets are divided. To address this concern, three-fold cross-validation, as shown in Fig. 17, was conducted.

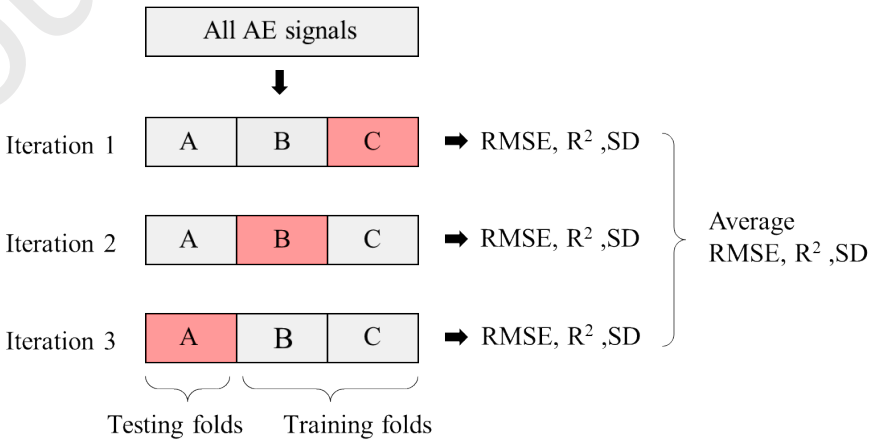

Fig. 17. Three-fold cross-validation

The experimentally collected AE signals were divided into three mutually exclusive subsets of equal size, namely A, B, and C. In the first iteration, the signals in A and B are selected as the training and validation sets, and the signals in C are used as the testing set. In the second iteration, the signals in B are employed as the testing set, and the remaining two subsets are used as the training and validation sets. In the third iteration, the signals in A are used as the testing set, and the other two subsets are used as the training and validation sets. After the three iterations are completed, all the RMSE, $R^{2,}$ and SD obtained from the three iterations are averaged and used to evaluate the performance of source localization. In this way, all signals are involved in the training and testing, which allows the quality of the model to be evaluated effectively while also avoiding overfitting and underfitting. The performances of all the models in this paper (single regression-based CNN using different images, ER-CNN, and WER-CNN) are examined by the three-fold cross-validation. Details are listed in Tables 4, 5, and 6.

Table 4. RMSE (meters) of three-fold cross-validation

Coordinates	Train/ Testing	CNN Input: STFT	CNN Input: Fusion	CNN Input: CWT	ER-CNN no weight	WER-CNN with weight
Coordinate *X*	(A, B), C	0.084	0.079	0.075	0.056	0.054
	(A, C), B	0.088	0.082	0.078	0.061	0.055
	(B, C), A	0.085	0.079	0.072	0.057	0.054
	Average	**0.086**	**0.080**	**0.075**	**0.058**	**0.054**
Coordinate *Y*	(A, B), C	0.058	0.053	0.043	0.035	0.032
	(A, C), B	0.057	0.052	0.043	0.033	0.029
	(B, C), A	0.057	0.054	0.045	0.035	0.031
	Average	**0.057**	**0.053**	**0.044**	**0.034**	**0.031**

Table 5. R^2 of three-fold cross-validation

Coordinates	Train/ Testing	CNN Input: STFT	CNN Input: Fusion	CNN Input: CWT	ER-CNN no weight	WER-CNN with weight
Coordinate *X*	(A, B), C	0.9975	0.9971	0.9979	0.9985	0.9988
	(A, C), B	0.9970	0.9966	0.9971	0.9981	0.9985
	(B, C), A	0.9974	0.9960	0.9978	0.9983	0.9986
	Average	**0.9973**	**0.9966**	**0.9979**	**0.9983**	**0.9986**
Coordinate *Y*	(A, B), C	0.9925	0.9894	0.9941	0.9962	0.9967
	(A, C), B	0.9914	0.9901	0.9932	0.9962	0.9968
	(B, C), A	0.9914	0.9902	0.9934	0.9960	0.9964
	Average	**0.9918**	**0.9899**	**0.9935**	**0.9961**	**0.9966**

Table 6. Standard deviation (meters) of three-fold cross-validation

Coordinates	Train/ Testing	CNN Input: STFT	CNN Input: Fusion	CNN Input: CWT	ER-CNN no weight	WER-CNN with weight
Coordinate *X*	(A, B), C	0.061	0.063	0.048	0.037	0.036
	(A, C), B	0.064	0.066	0.053	0.038	0.037
	(B, C), A	0.061	0.067	0.049	0.038	0.037
	Average	**0.062**	**0.065**	**0.050**	**0.038**	**0.037**
Coordinate *Y*	(A, B), C	0.042	0.045	0.035	0.026	0.024
	(A, C), B	0.041	0.044	0.034	0.025	0.024
	(B, C), A	0.042	0.044	0.036	0.026	0.024
	Average	**0.042**	**0.044**	**0.035**	**0.026**	**0.024**

The RMSE, $R^{2,}$ and SD obtained for all three iterations of the models in this paper are stable and close to the average value. Furthermore, the proposed WER-CNN model shows a performance that outperforms both single regression-based CNN and ER-CNN

in all three iterations. These indicate that the models in this paper are stable, and the source localization performance does not vary with the division of training and testing set.

4. 4. Computing time

Table 6 compares and presents the computational times of the proposed WER-CNN and the single CNN models utilizing the three types of inputs. The testing time in the table is the amount of time the model takes to localize a single signal in the test dataset. The findings showed that the training duration of WER-CNN (12033.6 s) is longer than those of single CNN models. The CNN utilizing STFT images has the shortest training time of the three single CNN models, whereas the CNN using CWT images has the longest. In the field application, Since the models will be trained offline, training time would not be a major concern. The trained model would be used to perform source localization in the field, therefore testing time would be the primary concern. According to Table 7, the trained models can estimate the coordinates very quickly. All trained models can complete the estimation in less than one second. Indicating that the models can be appropriate for field SHM.

Table 7. Summary of computing times

Model	Training time (s)	Testing time (s)
WER-CNN	12033.6	0.77
CNN, Input: WFE-fusion	800.9	0.05
CNN, Input: STFT	789.5	0.05
CNN, Input: CWT	819.1	0.06

5. Conclusions

This paper describes an approach to detect damage in stainless steel spent fuel storage canisters through AE monitoring and localizing the damage with only one AE sensor attached. A weighted ensemble regression-based CNN, which consists of multiple single regression-based CNN models, was proposed to analyze the AE signals from one sensor and derive the coordinates of the damage source. Three types of input images, including the WFE-fusion images, STFT images, and CWT images, were created based on AE signals. To evaluate the effectiveness of the proposed method, a large-scale 304 stainless steel specimen, which has a similar length and thickness to the actual canister, was used as an experimental specimen to collect AE signals and validate the proposed approach. Three metrics: RMSE, R^2, and standard deviation, were employed to quantify the performance of source localization. In addition, three-fold cross-validation was conducted to eliminate the influence brought by overfitting and underfitting, as well as to evaluate the effectiveness of the method more comprehensively. The main conclusions are summarized as follows:

- The source localization performances of the single regression-based CNN models were tested by respectively using WFE-fusion images, STFT images, and CWT images as the input. Results suggest that the single regression-based CNN model

using STFT has the relevant worse performance in terms of RMSE, R^2, and standard deviation. Concurrently the model using CWT images has the best performance.

- The source localization performance of the proposed WER-CNN was investigated. Results indicate that the weighted ensemble model shows significant improvement in RMSE, R^2, and standard deviation over the single regression-based model.
- The effect of the weighted average mechanism used in the WER-CNN was studied. By removing the mechanism, a decrease in the source localization performance can be observed in the ER-CNN model, which indicates the effectiveness of the weighted averaging mechanism.
- The results of three-fold cross-validation imply that both the single regression-based CNN models using three types of input images and the ensemble regression-based CNN models using all images are stable and do not vary with the division of training and testing set.

One of the limitations of the current study is that the proposed approach would only work for localizing signals on one plate-like steel specimen. To locate realistic SCC damage in future practical applications, the proposed localization method should be improved to adapt the actual canisters. And more AE signals collected from a number of different storage canisters should be included in the training data set to increase the generalization performance of the localization method. Only using one sensor to preliminarily verify the proposed method on a plate-like structure is also a limitation. For a plate-like structure, using only one sensor can yield good localization results. However, for a cylindrical structure such as the actual canister, at least two AE sensors may be required to achieve the same level of localization performance. Future research should further update the localization approach using two sensors and validate the approach on the actual spent fuel storage canisters. Another limitation may be that the uncertainty of the damage signal due to damage size, frequency dispersion, and etc. is not taken into consideration. The PLB signals may be similar which could also lead to generalization problems. It is recommended for the future study to do the following: (1) use different pinch angles for PLB; (2) add signals generated by the AE signal generator to the dataset; (3) add numerical simulated signals dataset.

Acknowledgment

This research was partially supported by Electric Power Research Institute (EPRI) under project number 1-108781, and the U.S Department of Energy-Nuclear Energy University Program (NEUP) under the contract DE-NE0008544. The views and opinions of the authors expressed herein do not necessarily state or reflect the opinions of the funding agencies.

Data availability

The raw/processed data required to reproduce these findings can be made available upon a reasonable request and with the written permission of the sponsor.

References

[1] A. Macfarlane, 2001. Interim storage of spent fuel in the United States, Annual review of energy and the environment, 26, 201-235. https://doi.org/10.1146/annurev.energy.26.1.201.

[2] R. Alvarez, J. Beyea, K. Janberg, J. Kang, E. Lyman, A. Macfarlane, G. Thompson, F.N. von Hippel, 2003. Reducing the hazards from stored spent power-reactor fuel in the United States, Science and Global Security, 11, 1-51. https://doi.org/10.1080/08929880309006.

[3] F. Von Hippel, 2007, Managing spent fuel in the United States: The illogic of reprocessing, JSTOR.

[4] EPRI, 2016, Investigation of Acoustic Emission Technologies for Monitoring Inaccessible Regions of Dry Fuel Storage Systems, EPRI, Palo Alto, CA.

[5] T.S. Mintz, L. Miller, Y.-M. Pan, X. He, R. Pabalan, L. Caseres, G. Oberson, D. Dunn, 2013, Coastal Salt Effects on the Stress Corrosion Cracking of Type 304 Stainless Steel, OnePetro.

[6] A.B. Goumeidane, N. Nacereddine, M. Khamadja, 2015. Computer aided weld defect delineation using statistical parametric active contours in radiographic inspection, Journal of X-ray Science and Technology, 23, 289-310. https://doi.org/10.3233/XST-150488.

[7] R. Chen, K.T. Tran, H.M. La, T. Rawlinson, K. Dinh, 2022. Detection of delamination and rebar debonding in concrete structures with ultrasonic SH-waveform tomography, Automation in Construction, 133, 104004. https://doi.org/10.1016/j.autcon.2021.104004.

[8] L. K C, A. Ross, L. Ai, A. Henderson, E. Elbatanouny, M. Bayat, P. Ziehl, 2023. Determination of vehicle loads on bridges by acoustic emission and an improved ensemble artificial neural network, Construction and Building Materials, 364, 129844. https://doi.org/10.1016/j.conbuildmat.2022.129844.

[9] L. Ai, V. Soltangharaei, R. Anay, M.J. van Tooren, P. Ziehl, 2020, Data-driven source localization of impact on aircraft control surfaces, IEEE, 1-10. https://doi.org/10.1109/AERO47225.2020.9172742.

[10] L. Ai, B. Greer, J. Hill, V. Soltangharaei, R.A.P. Ziehl, 2019, Finite element modeling of acoustic emission in dry cask storage systems generated by cosine bell sources, AIP Publishing LLC, 130001. https://doi.org/10.1063/1.5099851.

[11] D. Han, Y. Zhao, Y. Pan, G. Liu, T. Yang, 2020. Heating process monitoring and evaluation of hot in-place recycling of asphalt pavement using infrared thermal imaging, Automation in Construction, 111, 103055. https://doi.org/10.1016/j.autcon.2019.103055.

[12] K.R. Ramakrishnan, S. Corn, N. Le Moigne, P. Ienny, P. Slangen, 2021. Experimental assessment of low velocity impact damage in flax fabrics reinforced biocomposites by coupled high-speed imaging and DIC analysis, Composites Part A: Applied Science and Manufacturing, 140, 106137. https://doi.org/10.1016/j.compositesa.2020.106137.

[13] V. Soltangharaei, R. Anay, L. Ai, E.R. Giannini, J. Zhu, P. Ziehl, 2020. Temporal evaluation of ASR cracking in concrete specimens using acoustic

emission, Journal of Materials in Civil Engineering, 32, 04020285. https://doi.org/10.1061/(ASCE)MT.1943-5533.0003353.

[14] L. Ai, V. Soltangharaei, P. Ziehl, 2022. Developing a heterogeneous ensemble learning framework to evaluate Alkali-silica reaction damage in concrete using acoustic emission signals, Mechanical Systems and Signal Processing, 172, 108981. https://doi.org/10.1016/j.ymssp.2022.108981.

[15] L. Ai, V. Soltangharaei, P. Ziehl, 2021. Evaluation of ASR in concrete using acoustic emission and deep learning, Nuclear Engineering and Design, 380, 111328. https://doi.org/10.1016/j.nucengdes.2021.111328.

[16] C.B. Scruby, 1987. An introduction to acoustic emission, Journal of Physics E: Scientific Instruments, 20, 946. https://doi.org/10.1088/0022-3735/20/8/001.

[17] K.M. Holford, M.J. Eaton, J.J. Hensman, R. Pullin, S.L. Evans, N. Dervilis, K. Worden, 2017. A new methodology for automating acoustic emission detection of metallic fatigue fractures in highly demanding aerospace environments: An overview, Progress in Aerospace Sciences, 90, 1-11. https://doi.org/10.1016/j.paerosci.2016.11.003.

[18] V. Soltangharaei, J. Hill, L. Ai, R. Anay, B. Greer, M. Bayat, P. Ziehl, 2020. Acoustic emission technique to identify stress corrosion cracking damage, Structural Engineering and Mechanics, 75, 723-736. https://doi.org/10.12989/sem.2020.75.6.723.

[19] M. Khyzhniak, M. Malanowski, 2021, Localization of an Acoustic Emission Source Based on Time Difference of Arrival, IEEE, 117-121. https://doi.org/10.1109/SPSympo51155.2020.9593909.

[20] M.I. Jordan, T.M. Mitchell, 2015. Machine learning: Trends, perspectives, and prospects, Science, 349, 255-260. https://doi.org/10.1126/science.aaa841.

[21] I. Goodfellow, Y. Bengio, A. Courville, 2016. Machine learning basics, Deep learning, 1, 98-164.

[22] A. Mohammadi, J.H. Gull, R. Taghinezhad, A. Azizinamini, 2014. Assessment and evaluation of timber piles used in Nebraska for retrofit and rating.

[23] Y. Tang, Y. Guo, X. Chen, Z. Wang, Y. Wei, 2022. Acoustic emission characteristics of concrete cylinders reinforced with steel-fiber-reinforced composite bars under uniaxial compression, Journal of Building Engineering, 59, 105074. https://doi.org/10.1016/j.jobe.2022.105074.

[24] I. Goodfellow, Y. Bengio, A. Courville, Y. Bengio, 2016, Deep learning, MIT press Cambridge.

[25] Q. Zhang, K. Barri, S.K. Babanajad, A.H. Alavi, 2020. Real-time detection of cracks on concrete bridge decks using deep learning in the frequency domain, Engineering. https://doi.org/10.1016/j.eng.2020.07.026.

[26] J. Dahlberg, B. Phares, J. Bigelow, F.W. Klaiber, 2012, Timber abutment piling and back wall rehabilitation and repair.

[27] C.U. Grosse, M. Ohtsu, D.G. Aggelis, T. Shiotani, 2021, Acoustic emission testing: Basics for research–applications in engineering, Springer Nature.

[28] S.H. Jambukia, V.K. Dabhi, H.B. Prajapati, 2015, Classification of ECG signals using machine learning techniques: A survey, IEEE, 714-721.

https://doi.org/10.1109/ICACEA.2015.7164783.

[29] D.G. Aggelis, T. Shiotani, in, Acoustic Emission Testing, Springer, 2022, pp. 45-71.

[30] Y. Lei, B. Yang, X. Jiang, F. Jia, N. Li, A.K. Nandi, 2020. Applications of machine learning to machine fault diagnosis: A review and roadmap, Mechanical Systems and Signal Processing, 138, 106587. https://doi.org/10.1016/j.ymssp.2019.106587.

[31] T. Suzuki, S. Nishimura, Y. Shimamoto, T. Shiotani, M. Ohtsu, 2020. Damage estimation of concrete canal due to freeze and thawed effects by acoustic emission and X-ray CT methods, Construction and Building Materials, 245, 118343. https://doi.org/10.1016/j.conbuildmat.2020.118343.

[32] M.A. Meier, Z.E. Ross, A. Ramachandran, A. Balakrishna, S. Nair, P. Kundzicz, Z. Li, J. Andrews, E. Hauksson, Y. Yue, 2019. Reliable real-time seismic signal/noise discrimination with machine learning, Journal of Geophysical Research: Solid Earth, 124, 788-800. https://doi.org/10.1029/2018JB016661.

[33] A. Ebrahimkhanlou, B. Dubuc, S. Salamone, 2019. A generalizable deep learning framework for localizing and characterizing acoustic emission sources in riveted metallic panels, Mechanical Systems and Signal Processing, 130, 248-272. https://doi.org/10.1016/j.ymssp.2019.04.050.

[34] L. Ai, V. Soltangharaei, M. Bayat, M. van Tooren, P. Ziehl, 2021. Detection of impact on aircraft composite structure using machine learning techniques, Measurement Science and Technology, 32, 084013. https://doi.org/10.1088/1361-6501/abe790.

[35] L. Ai, V. Soltangharaei, M. Bayat, B. Greer, P. Ziehl, 2021. Source localization on large-scale canisters for used nuclear fuel storage using optimal number of acoustic emission sensors, Nuclear Engineering and Design, 375, 111097. https://doi.org/10.1016/j.nucengdes.2021.111097.

[36] L. Yang, F. Xu, 2020. A novel acoustic emission sources localization and identification method in metallic plates based on stacked denoising autoencoders, IEEE Access, 8, 141123-141142. https://doi.org/10.1109/ACCESS.2020.3012521.

[37] T. Boczar, M. Lorenc, 2004. Determining the repeatability of acoustic emission generated by the Hsu-Nielsen calibrating source, Molecular and quantum Acoustics, 25, 177-192.

[38] H.J. Nussbaumer, in, Fast Fourier Transform and Convolution Algorithms, Springer, 1981, pp. 80-111.

[39] A. Wehrl, 1978. General properties of entropy, Reviews of Modern Physics, 50, 221. https://doi.org/10.1103/RevModPhys.50.221

[40] C.E. Shannon, 2001. A mathematical theory of communication, ACM SIGMOBILE mobile computing and communications review, 5, 3-55.

[41] C.E. Shannon, 1948. A mathematical theory of communication, The Bell system technical journal, 27, 379-423. https://doi.org/10.1002/j.1538-7305.1948.tb01338.x.

[42] M. Mousavi, D. Holloway, J. Olivier, A.H. Alavi, A.H. Gandomi, 2019. A

Shannon entropy approach for structural damage identification based on self-powered sensor data, Engineering Structures, 200, 109619. https://doi.org/10.1016/j.engstruct.2019.109619.

[43] L. Durak, O. Arikan, 2003. Short-time Fourier transform: two fundamental properties and an optimal implementation, IEEE Transactions on Signal Processing, 51, 1231-1242. https://doi.org/10.1109/TSP.2003.810293.

[44] W. Zhou, Z. Feng, Y. Xu, X. Wang, H. Lv, 2022. Empirical Fourier decomposition: An accurate signal decomposition method for nonlinear and non-stationary time series analysis, Mechanical Systems and Signal Processing, 163, 108155. https://doi.org/10.1016/j.ymssp.2021.108155.

[45] B. Shi, M. Cao, Z. Wang, W. Ostachowicz, 2022. A directional continuous wavelet transform of mode shape for line-type damage detection in plate-type structures, Mechanical Systems and Signal Processing, 167, 108510. https://doi.org/10.1016/j.ymssp.2021.108510.

[46] J.M. Lilly, S.C. Olhede, 2012. Generalized Morse wavelets as a superfamily of analytic wavelets, IEEE Transactions on Signal Processing, 60, 6036-6041. https://doi.org/10.1109/TSP.2012.2210890.

[47] J.M. Lilly, S.C. Olhede, 2008. Higher-order properties of analytic wavelets, IEEE Transactions on Signal Processing, 57, 146-160. https://doi.org/10.1109/TSP.2008.2007607.

[48] A. Krizhevsky, I. Sutskever, G.E. Hinton, 2012, Imagenet classification with deep convolutional neural networks, 1097-1105. https://doi.org/10.1145/3065386.

[49] D. Li, Y. Wang, W.-J. Yan, W.-X. Ren, 2020. Acoustic emission wave classification for rail crack monitoring based on synchrosqueezed wavelet transform and multi-branch convolutional neural network, Structural Health Monitoring, 1475921720922797. https://doi.org/10.1177/1475921720922797.

[50] J.C. Garrett, H. Mei, V. Giurgiutiu, 2022. An artificial intelligence approach to fatigue crack length estimation from acoustic emission waves in thin metallic plates, Applied Sciences, 12, 1372. https://doi.org/10.3390/app12031372.

[51] N.C. Oza, S.J. Russell, 2001, Online bagging and boosting, PMLR, 229-236.

Highlights:

- A data fusion method is presented, which integrates AE waveform, FFT spectrum, and spectral entropy.
- A weighted ensemble regression-based CNN was proposed to estimate the coordinates of damage.
- Fusion data, CWT, and STFT coefficients were used as input data.
- The proposed model estimates the coordinates of damages with high performance.

Declaration of interests

Dear Prof. Paolo Carbone,

Editors-in-Chief of Measurement

Please find the enclosed manuscript co-authored by :

Li Ai, Mahmoud Bayat, Paul Ziehl

Entitled: **Localizing Damage on Stainless Steel Structures Using Acoustic Emission Signals and Weighted Ensemble Regression-based Convolutional Neural Network**

☒ The authors declare that they have no known competing financial interests or personal relationships that could have appeared to influence the work reported in this paper.

☐The authors declare the following financial interests/personal relationships which may be considered as potential competing interests:

Sincerely yours,

Mahmoud Bayat

Mahmoud Bayat, Ph.D.
Research Associate Professor, Department of Mechanical Engineering, University of South Carolina, Columbia, SC, USA
Editor, ASCE Journal of Practice Periodical on Structural Design and Construction
Editor, Journal of Low-Frequency Noise, Vibration and Active Control
Tel: +1(412)418-2208 : Email: mbayat@mailbox.sc.edu